AGU PUBLICATIONS

Geophysical Research Letters

Supporting Information for

Exacerbation of the 2013–2016 Pan-Caribbean Drought by Anthropogenic Warming

D. A. Herrera[1*], T. R. Ault[1], J. T. Fasullo[2], S. J. Coats[3], C. M. Carrillo[1], B. I. Cook[4], and A. P. Williams[5]

[1]Department of Earth and Atmospheric Sciences, Cornell University, Ithaca, 14853, NY, USA.

[2] Climate and Global Dynamics Division, National Center for Atmospheric Research, 3090 Center Green Dr., Boulder, CO, 80301, USA.

[3] Woods Hole Oceanographic Institution, 266 Woods Hole Rd., Woods Hole, 02543-1050, MA, USA.

[4] NASA Goddard Institute for Space Studies, 2880 Broadway, New York, NY, USA.

[5] Lamont-Doherty Earth Observatory of Columbia University, 61 Route 9W, Palisades, 10964, NY, USA.

Contents of this file

Text S1 to S8
Figures S1 to S8
Tables S1 to S3

Introduction

This document further describes the methods and findings of our work. We have included a more comprehensive description of the metrics we used here to estimate the contributions of anthropogenic warming to the Pan-Caribbean drought.

S1. Climate data

The observed and simulated climate products we used to calculate PET and scPDSI are listed in the Tables S1 and S2. Because of the relatively coarse horizontal resolution of the current gridded climate products, which varies from 0.5º to 2.5º (~55 km to ~280 km, respectively) and fails to resolve many of the Lesser Antilles (Jury et al., 2007; Dai, 2011; 2013; van der Schrier et al., 2013; Cook et al., 2015), we used statistically-downscaled monthly precipitation data from the Global Precipitation Climatology Centre (GPCC) "combined product" (available at: https://www.esrl.noaa.gov/psd/data/gridded/data.gpcc.html)(Schneider et al., 2015a,b), and temperature fields (T_{min}, T_{mean}, and T_{max}) from the Berkeley Earth Surface Temperature (BEST) (Rohde et al., 2013). Wind speed and net radiation data were obtained from National Centers for Environmental Predictions–National Center for Atmospheric Research (NCEP–NCAR) (Kalnay et al., 1996) and the Japanese 55-year (JRA-55) (Ebita et al., 2011) reanalyses, and were bi-linearly interpolated to a common resolution of 4 km. The validation of downscaled products and further details of the downscaling and bias-correction procedures we used are described in the Supporting Information and in Herrera and Ault (2017). We also computed alternate PET and scPDSI records based on data from the Climatic Research Unit version TS4.01 (CRU vTS4.01) (Harris et al., 2014) and found that results were nearly identical to those reported here. To carefully assess the role of radiative flux on drought variability, we used observed surface radiation (up and down, shortwave and long wave) and cloud-cover data from the Clouds and Earth's Radiant Energy System (CERES) (Loeb et al., 2012) at 1º geographic resolution spanning January 2001/December 2016. CERES data were not used to calculate PET nor scPDSI, but rather to conduct a complementary analysis of observed radiative fluxes during the Pan-Caribbean drought.

Simulated temperature data (T_{min} and T_{max}) were obtained from the Coupled Model Intercomparison Project Phase 5 (CMIP5) (Taylor et al., 2012) and are listed in Table S2. Models were selected based solely on the availability of monthly T_{min} and T_{max} data during the study interval. We used temperature data from the archive's historical simulations from 1950 to 2005, appended to the Representative Concentrations Pathway 8.5 (RCP8.5) to cover 2006/2016. Pre-industrial control and naturally-forced historical simulations were used as a benchmark to estimate the contribution of anthropogenic-forcing to scPDSI and PET-anomalies. CMIP5 data of precipitation, net radiation, wind speed, and soil moisture were further used to assess the consistency of scPDSI with simulated soil moisture in terms of interannual variability and long-term trends. CMIP5 model data used in this work were obtained from https://esgfnode.llnl.gov/search/esgf-llnl/, and in contrast to GPCC and BEST, CMIP5 climate data were not downscaled.

S2. The self-Calibrating Palmer Drought Severity Index

The original PDSI consists of a simple water balance model that uses precipitation and PET as moisture supply and demand, respectively, coupled with a two-layer soil model (Palmer, 1965). Despite its successful use in diagnosing drought during recent decades, the PDSI yields inconsistent results across climates (Alley, 1984). This issue is largely due to the constant duration factors in the original PDSI formulation, which were empirically derived from stations in the central US (Palmer, 1965; Alley, 1984; Wells et al., 2004). scPDSI addresses this limitation by automatically calculating duration factors based on local climate conditions during a determined calibration period (Wells et al., 2004). The PDSI's calibration period is the interval used to establish the normal hydroclimatic conditions for a specific location (Palmer, 1965), and hence partially controls the variance of the index. scPDSI is calculated with the same basic formulation as the original PDSI as:

$$\mathrm{X_i} = \mathrm{pX_{i-1}} + \mathrm{qZ_i}, \tag{1}$$

where X_i is the index value in month i, $X_{i\text{-}1}$ is the index of the previous month, p and q are the duration factors, and Z_i is the current moisture anomaly. The duration factors determine the autocorrelation of the PDSI by assigning different weights to$X_{i\text{-}1}$ and Z_i to determine the current index. As suggested in Dai (2011; 2013), we used a 1950/1980 calibration period in our scPDSI computations because the anthropogenic signal is more pronounced after the 1980s. However, because the JRA-55 reanalysis spans 1958/near present, we used a 1958/1980 period in our estimations with JRA-55. Further details on how we calculated scPDSI are described by Herrera and Ault (2017).

S3. The FAO reference evapotranspiration

We used a modified version of the original Penman-Monteith (PM) method, as used by the UN Food and Agricultural Organization (FAO) (Allen et al., 1998). We selected this method because it requires fewer inputs for its computation as compared to the original PM method (Penman, 1948; Monteith, 1965; Allen et al., 1998), which is advantageous for regions where climate data are sparse such as the Caribbean. The theoretical basis of the FAO-PM method lies in an idealized grass-surface with a permanent water supply and 0.12 m height. It also assumes a soil resistance of 70 s m^{-1}, and a surface albedo of 0.23 (Allen et al., 1998). Formally, PET is calculated with the following equation:

$$PET = \frac{0.408\Delta(Rn-G)+\gamma\frac{900}{T+273.16}U_2(e_s-e_a)}{\Delta+\gamma(1+0.34U_2)}, \tag{2}$$

where,

$$U_2 = U_{10} \frac{\ln(128)}{\ln(661.3)}$$

PET is the crop reference evapotranspiration (mm day^{-1}), Rn is the net radiation (MJ m^{-2} d^{-1}), T is the average temperature at 2 m height (ºC), G is the soil heat flux density (MJ m^{-2} d^{-1}), U_2 is the wind speed measured (or estimated from U_{10}) at 2 m height (m s^{-1}), U_{10} is the wind speed measured at 10 m height (m s^{-1}), $e_s - e_a$ (e_s-e_a) is the vapor pressure deficit measured at 2 m height (kPa), Δ is the slope of the vapor pressure curve (kPa ºC^{-1}), γ is the psychrometric constant (kPa ºC^{-1}), 900 is the numerator coefficient for the reference crop (kJ^{-1} kg K d^{-1}), and 0.34 is the denominator coefficient for the reference crop (s m^{-1}) (Allen et al., 1998). In contrast to previous studies that used this method for calculating PET (Cook et al., 2015; 2016; Karnauskas et al., 2016), we estimated gridded saturated vapor pressure (e_s) using our downscaled and bias-corrected T_{max} and T_{min} products with the following equation (Allen et al., 1998):

$$e(T) = 0.6108 exp\left[\frac{17.27\,T}{T+237.3}\right], \quad (3)$$

where $e(T)$ is the vapor pressure (kPa) as a function of the air temperature, and T is the air temperature in degrees Celsius (ºC). The actual vapor pressure (e_a) was also obtained with Eq. (3) but using our downscaled T_{min} instead of dew-point temperature because we wanted to be consistent with (e_s), which was estimated with our downscaled temperature datasets. Also, we found that this simplification did not have meaningful impact on the results, as, when we calculated PET from reanalysis data, the Caribbean PET record was similar regardless of whether we calculated (e_a) from T_{min} or specific humidity. Furthermore, since we used our downscaled temperature datasets for these computations, the topographic influence to vapor pressure was therefore taken into account. This PET dataset is the same we used in Herrera and Ault (2017), and is currently available upon request.

S4. Anthropogenic contributions to drought severity

The contributions of anthropogenic warmth to the Pan-Caribbean drought were estimated using an array of observed gridded climate data, which were combined to validate the consistency of our findings. Specifically, we used the following combinations of (a) precipitation, (b) temperature (T_{min}, T_{mean}, and T_{max}), and (c) net-radiation (if available), total cloud cover, and wind speed to calculate PET and scPDSI:

a. GPCC "combined product", b. BEST, and c. JRA-55 reanalysis.
a. GPCC "combined product", b. BEST, and c. NCEP-NCAR reanalysis.
a., b., and c. CRU TS4.01
a. and b. CRU TS4.01, and c. JRA-55 reanalysis.

From each combination, we obtained the following contributions:

(1) ~14%, (2) ~16%, (3) ~15%, (4) ~13%, with a mean of ~14.5% and standard deviation of ~1.12%.

Contributions on each grid-cell were estimated using the following Equation:

$$\mathrm{C} = \left(1 - \left(\frac{\mathrm{PDSIdet}}{\mathrm{PDSIor}}\right)\right) * 100 \quad , \tag{4}$$

where C is the anthropogenic contribution, $\mathrm{PDSIdet}$ is PDSI calculated with adjusted temperatures (i.e., after the removal of the anthropogenic warming signal), while PDSIor is PDSI calculated using unadjusted temperature records.

S5. Statistical downscaling and validation of downscaled products

The downscaling method applied in this work is the same as in Herrera and Ault (2017), which similar to the "delta method" implemented by Mosier et al. (2014). To downscale temperature, we first calculated the anomalies of BEST dataset at its native resolution (1º lat/lon). Anomalies of maximum, minimum, and mean monthly temperatures were calculated with respect to the 1950–1980 climatology because the anthropogenic signal on temperature is more pronounced after the 1980s (Dai and Zhao, 2016; Zhao and Dai, 2016). These anomalies were then bilinearly interpolated to 4 km, and were then added to the WorldClim climatologies to generate downscaled temperature products with a spatial resolution of 4 km. Finally, we adjusted the annual temperature seasonality (WorldClim's standard deviation) so they match the WorldClim annual cycle.

To downscale precipitation, we applied a two-step using CHIRPS: 1) we re-gridded the original GPCC V7 dataset to match the resolution of CHIRPS (0.05º or ~6 km), and we then corrected the variances and means of GPCC so that they match with CHIRPS during the overlapping period from January 1981 to December 2015; 2) precipitation anomalies were calculated as the monthly fraction with respect to the 1950–1980 climatology; 3) these anomalies were bilinearly-interpolated and then aggregated to the WorldClim climatology to get a final downscaled product of 4 km (Herrera and Ault, 2017).

As in Herrera and Ault (2017), we validated our downscaled products before using them in our anthropogenic contribution estimations. To do so, we calculated the Spearman rank correlation and root-mean-square-errors (RMSE) between 38 weather stations and underlying grid cells for precipitation, and with 20 stations for mean temperature (Fig S3). Most of the weather stations used are from the Global Historical Climatology Network (GHCN), versions 2 and 3. As shown in Fig. S4, correlation coefficients between downscaled monthly precipitation and GHCN station range between $r = 0.76$ and $r = 0.97$, with an average of 0.89 over the Caribbean and northern South America. In terms of RMSE, we found the lowest value with the Maracaibo–Los Pozos station in Venezuela (RMSE = 27mm), and the highest in Caucagua, also in Venezuela (RMSE = 79mm). In terms of correlation coefficients and RMSE values with temperature fields (T_{min}, T_{mean}, and T_{max}), these were close to what we found with precipitation. The higher biases in mean temperature were found over mountainous regions in Hispaniola Island (RMSE = 0.91ºC), and northern South America (RMSE = 0.89ºC). Similar results were observed with monthly minimum and maximum temperature means, with RMSE ranging from 0.79º to 1.12ºC.

S6. ENSO-Caribbean drought

Some of the worst droughts in the Caribbean have been linked to the warm phase of El Niño–Southern Oscillation (ENSO; Peters, 2010; Blunden et al. 2016), including the 1997–1998, 2009–2010, and the 2013–2016 Pan-Caribbean drought. Although the dynamics between ENSO and Caribbean drought is not yet well constrained, previous studies have suggested that a persistent subsidence over northern South America could be responsible of the precipitation deficits observed during El Niño (Giannini et al. 2001a,b). In contrast, the usually wetter conditions observed in northwestern Cuba (e.g., Herrera and Ault, 2017), could be due to an increased intrusion of frontal systems during the boreal winter, when El Niño reaches its maximum intensity (e.g., Schultz et al. 1998; Giannini et al. 2001a,b). However, as described in Jury et al. (2007) and Herrera and Ault (2017), there is a seasonal dependency on ENSO effects to Caribbean precipitation. For example, during El Niño years precipitation deficits in the Caribbean are noticeable in early boreal autumn (ASO), when El Niño usually strengthens. In contrast, spring-summer (MJJ) of the year when El Niño is diminishing, it is usually associated to an even above-normal precipitation (Giannini et al. 2001a; Jury et al. 2007; Herrera and Ault, 2017). In addition, there is also a major geographic variability on ENSO effects to Caribbean precipitation (Jury et al. 2007; Herrera and Ault, 2017) (Fig. S5). ENSO seems to have a stronger influence in Western Caribbean precipitation variability (e.g., Cuba, Jamaica, and western Hispaniola Island), while the North Atlantic Oscillation (NAO)—although weaker—seems to have a more pronounced influence in Eastern-southeastern Caribbean (e.g., SE Lesser Antilles) (Jury et al. 2007). This is consistent with a recent study, in which the authors have found that ENSO effects to drought variability in Puerto Rico is not significant (Torres-Varcárcel, 2018).

S7. Observed surface radiative flux anomalies

Radiative changes during the Pan-Caribbean drought appear to have also played a role in its severity. Between 2013 and 2016, the average downwelling long-wave radiation (RLI) anomaly was 1.03 Wm^{-2}, while the downwelling short-wave radiation (RSI) was 1.84 Wm^{-2}. However, in 2015 when the drought peaked, RLI anomaly averaged 2.59 Wm^{-2} and RSI anomaly 3.22 Wm^{-2}. Above-normal anomalies in upwelling long and short-wave radiative fluxes (RLO and RSO) were also observed during the drought, with 1.2 and 0.11 Wm^{-2}, respectively. Given the relatively short time span covered by CERES (2001–present) it was not possible to assess the direct impact of anthropogenic climate change on surface radiative flux anomalies using this dataset. However, these analyses provide further insights into the radiative characteristics of the Pan-Caribbean drought. Additionally, CERES' cloud's fraction and optical depth reveal a below-normal cloud coverage and a persistent decrease in deep-convection across the Caribbean (Figs. S7 and S8), consistent with observed radiative flux and precipitation anomalies during the Pan-Caribbean drought.

S8. Supporting references

Bosart L. F., 1998: Planetary and synoptic-scale signatures associated with Central American cold surges. *Mon Wea Rev* 126:5–27.

Giannini, A., M. A. Cane, and Y. Kushnir, 2001a: Interdecadal changes in the ENSO teleconnection to the Caribbean region and the North Atlantic Oscillation. *J. Climate*, 14, 2867–2879, doi:10.1175/1520-0442(2001)014,2867:ICITET.2.0.CO;2.

——, J. C. Chiang, M. A. Cane, Y. Kushnir, and R. Seager, 2001b: The ENSO teleconnection to the tropical Atlantic Ocean: Contributions of the remote and local SSTs to rainfall variability in the tropical Americas. *J. Climate*, 14, 4530–4544, doi:10.1175/1520-0442(2001)014,4530:TETTTT.2.0.CO;2.Schultz DM, Bracken WE, Peters E. J., 2015: The 2009/2010 Caribbean drought: A case study. *Disasters* 39:738–761.

Torres-Varcárcel A. R., 2018: Teleconnections between ENSO and rainfall and drought in Puerto Rico. *Int J of Climatol* doi:10.1002/joc.5444.

SUPPORTING FIGURES

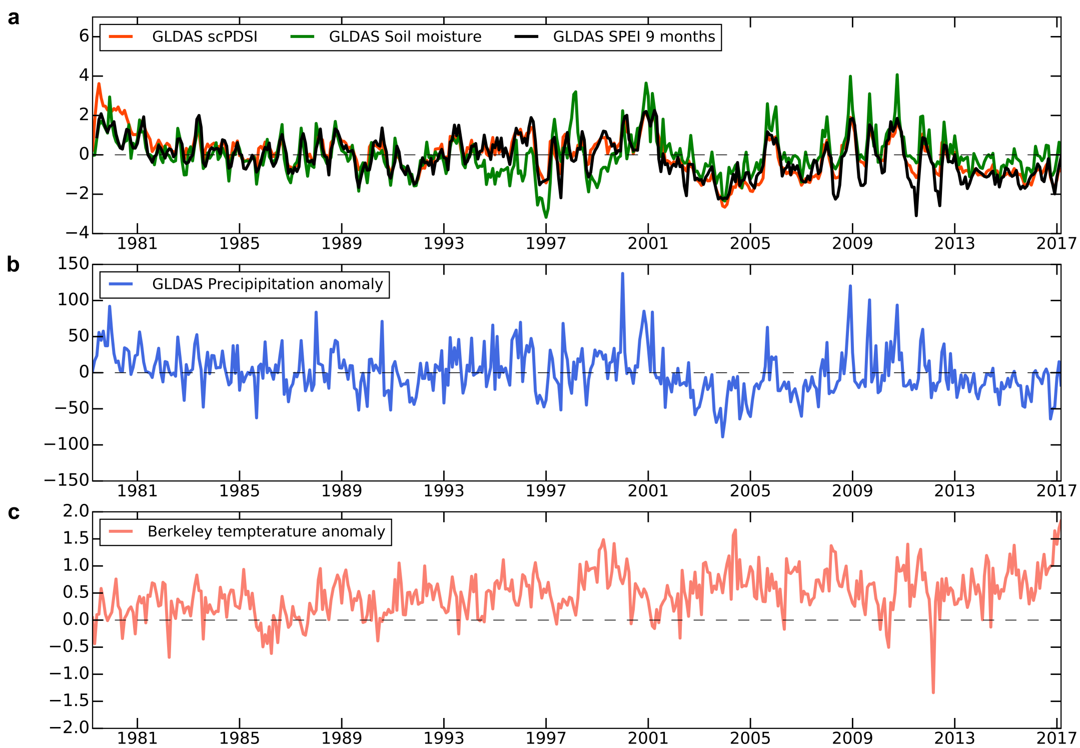

Figure S1. Water balance estimates using data from the Global Land Data Assimilation System (GLDAS). The metrics used here: (**a**) soil moisture anomalies (GLDAS Soil moisture), the self-calibrating Palmer Drought Severity Index (scPDSI; GLDAS scPDSI) and the Standardized Precipitation-Evapotranspiration Index (SPEI; GLDAS SPEI 9 months). All water balance metrics are consistent in terms of hydroclimate trends and variability during the 1979–2017 period. scPDSI and SPEI were calculated using precipitation data from GLDAS (**b**), and temperature from the Berkeley dataset (**c**). Precipitation and temperature anomalies are shown in mm and Celsius degrees, respectively.

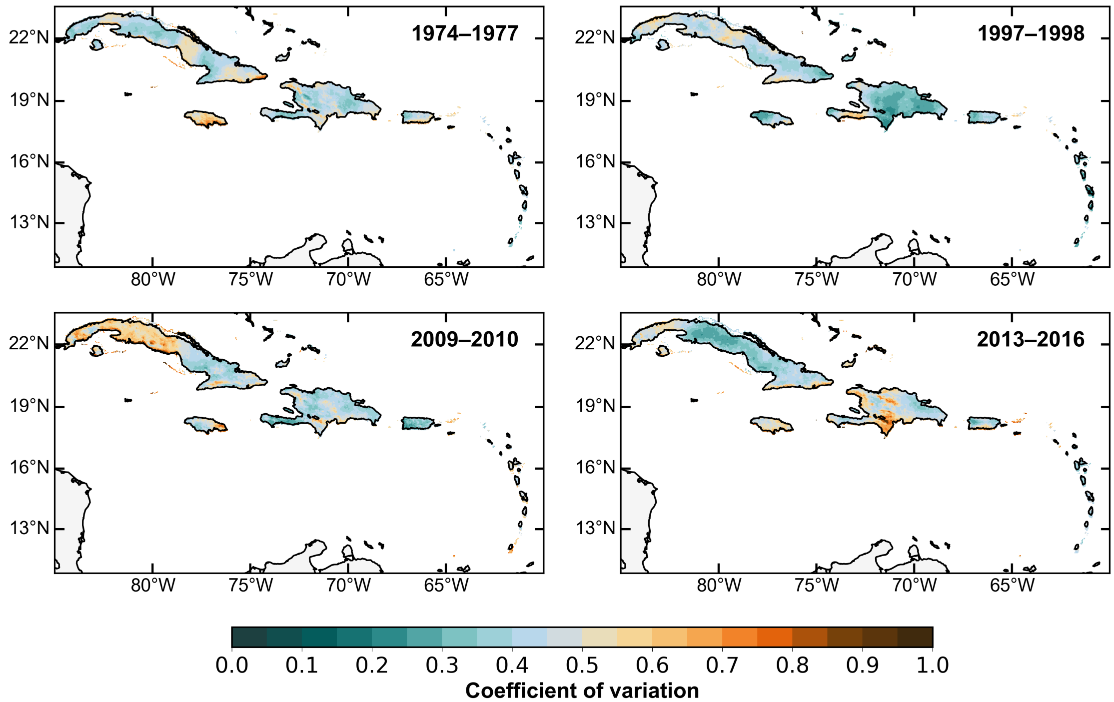

Figure S2. Coefficient of variation in precipitation anomalies during some of the worst droughts in the Caribbean. In 2013–2016, lower coefficients of variation are observed over the regions with the highest anthropogenic contributions on the drought.

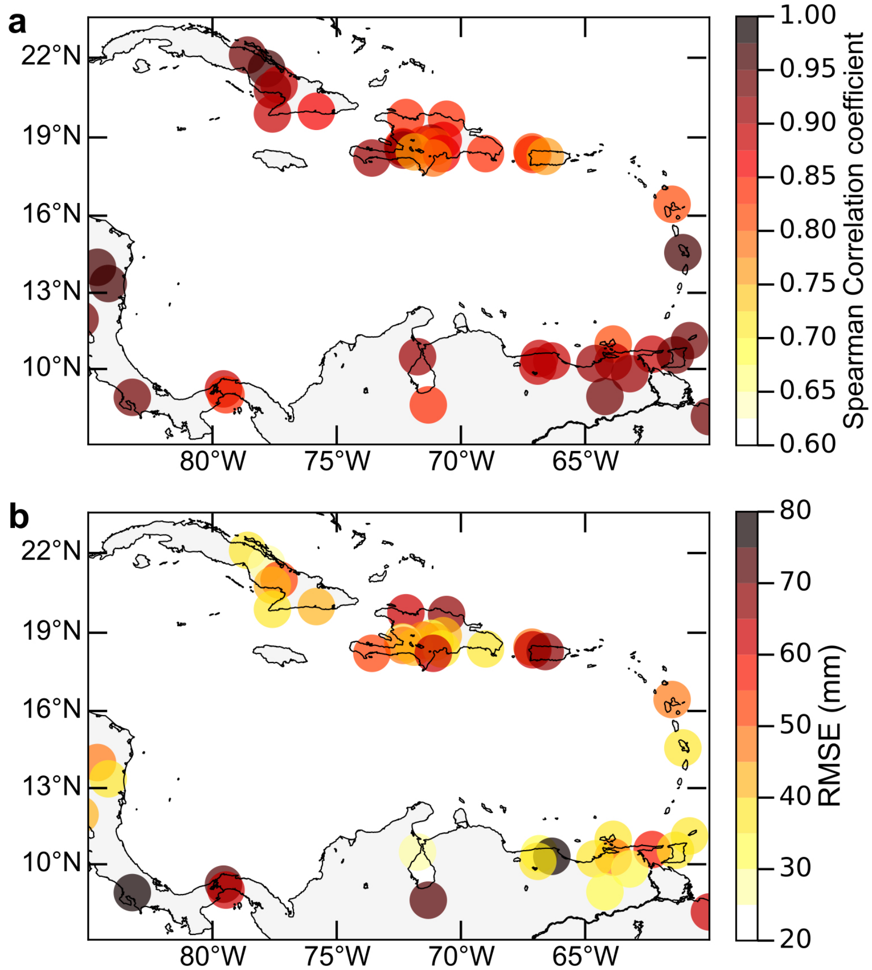

Figure S3. (a) Spearman rank correlation coefficients and **(b)** RMSE between our downscaled precipitation product and GHCN station data. The intervals of these correlations and RMSEs vary depending on the length of GHCN used. However, we selected stations with at least 20 years of continuous data.

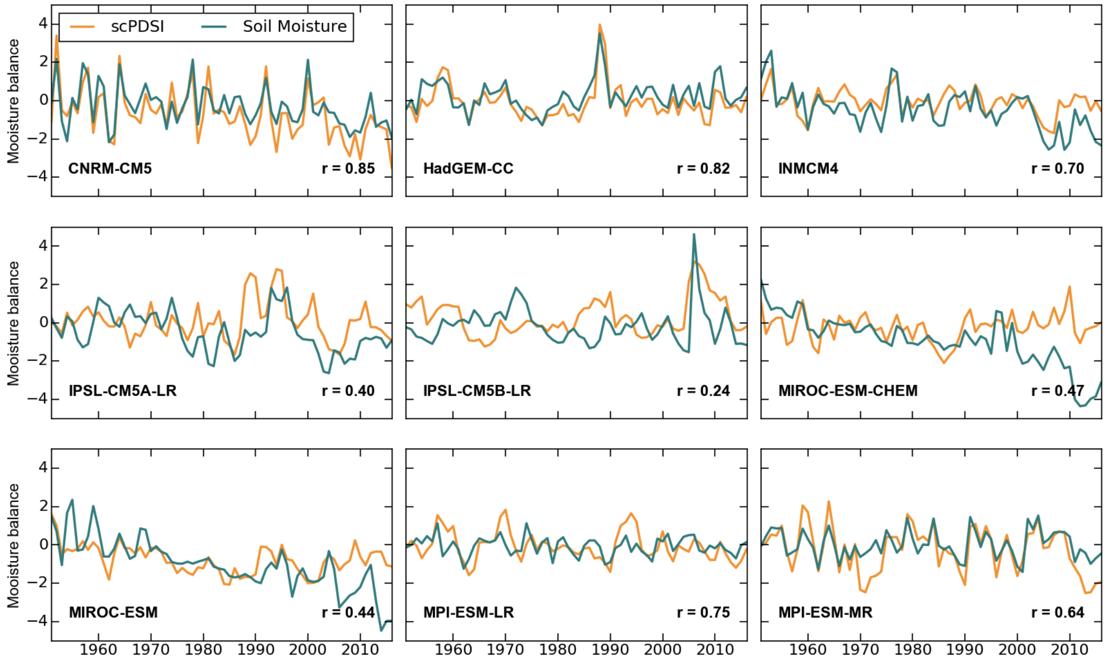

Figure S4. Simulated scPDSI and soil moisture anomalies during 1950–2016 from CMIP5. scPDSI significantly correlates with soil moisture anomalies in spite of the simple water balance model it uses. The significant correlations between these moisture balance indicators suggest that CO_2 fertilization plays a minor role in affecting PET in the Caribbean during the 1950–2016 interval.

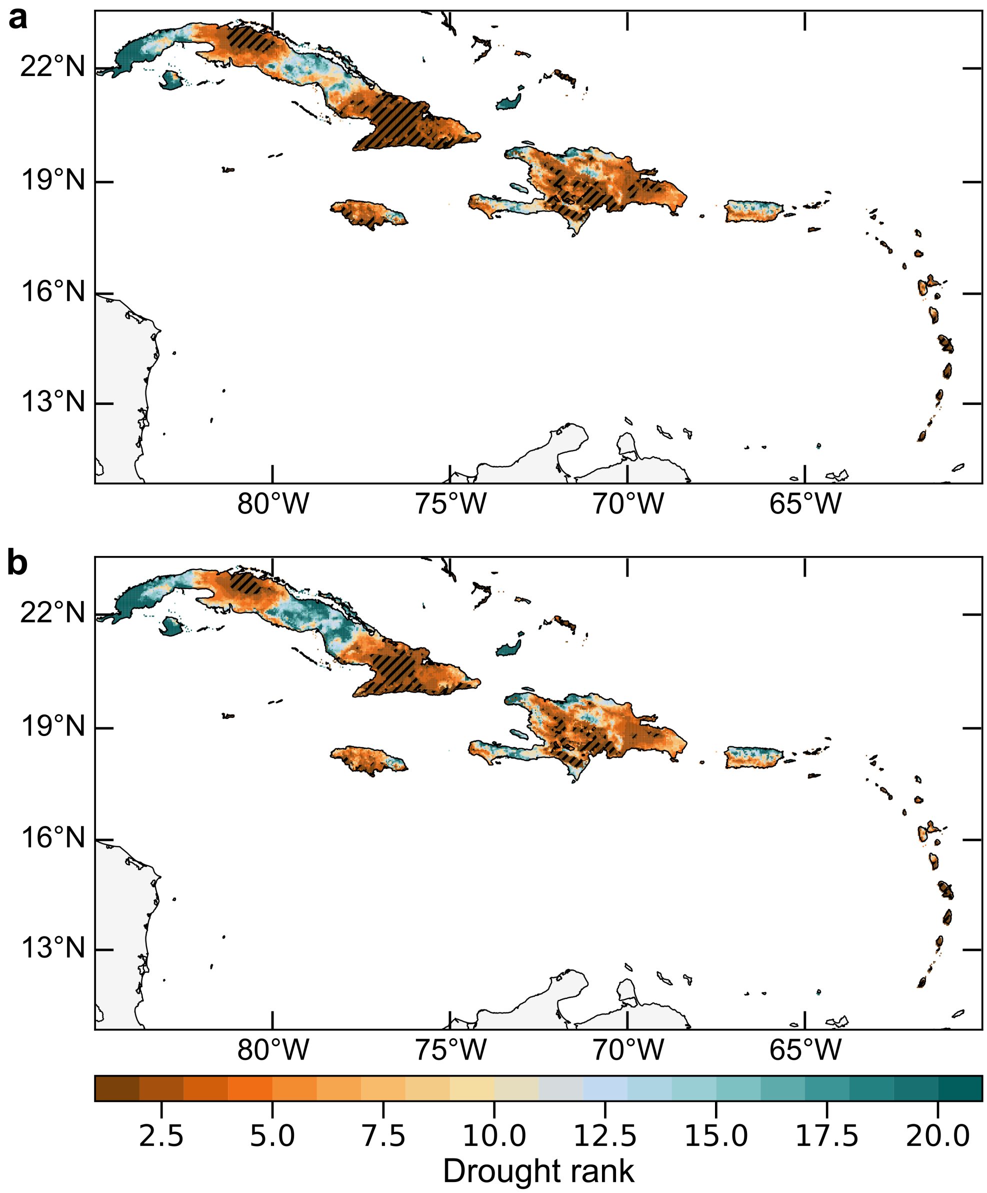

Figure. S5. Drought ranks of scPDSI estimated with the observed trend in temperature and adjusted temperatures. **(a)** Drought rankings of using the observed temperature trend. The hatching refers to the area where the Pan-Caribbean drought was record breaking any year between 2013 and 2016, which is nearly 32%. **(b)** As in (a) but using adjusted temperatures to calculate PET and scPDSI. In this case, the area where the Pan-Caribbean drought was record-breaking is ~21%.

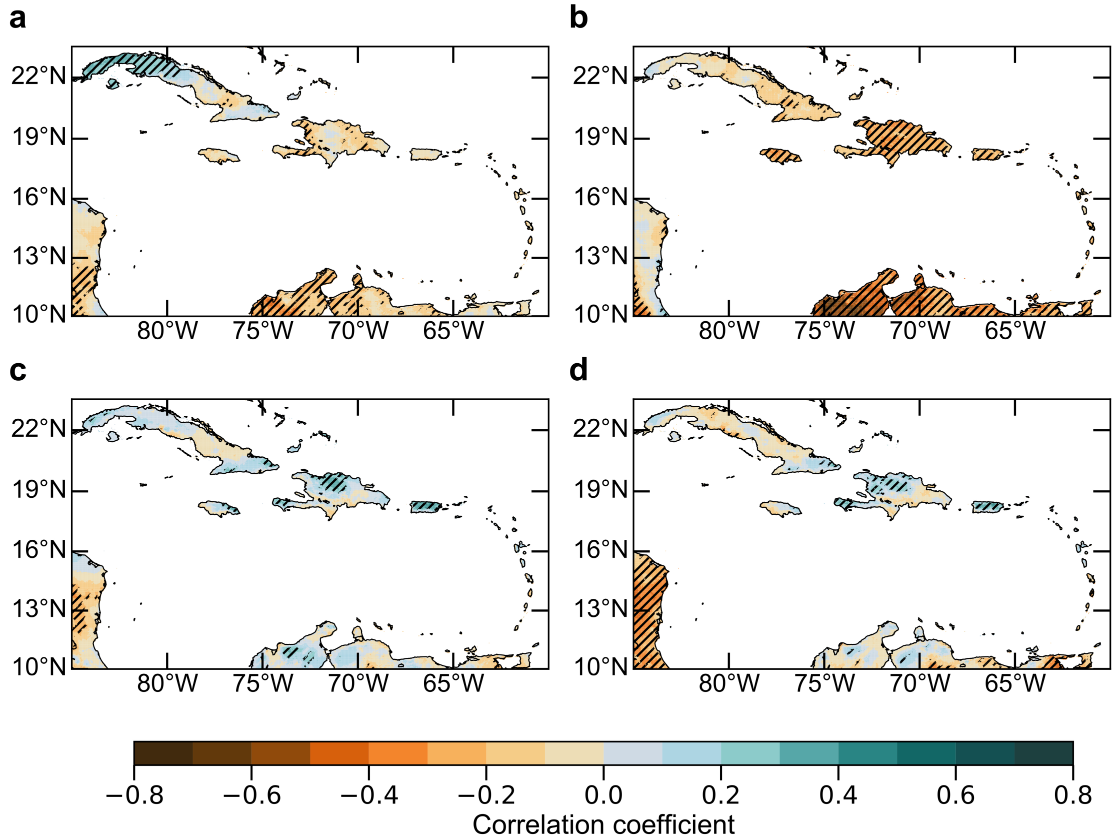

Figure S6. Correlations coefficients between our downscaled scPDSI and sea surface temperature anomalies (SSTAs) in the Niño-3.4 region. **(a)** In MJJ, **(b)** in ASO. **(c)**, **(d)** As in (a) and (b) but with SSTAs in the tropical North Atlantic. The hatched areas are statistically significant correlations at the 95% level.

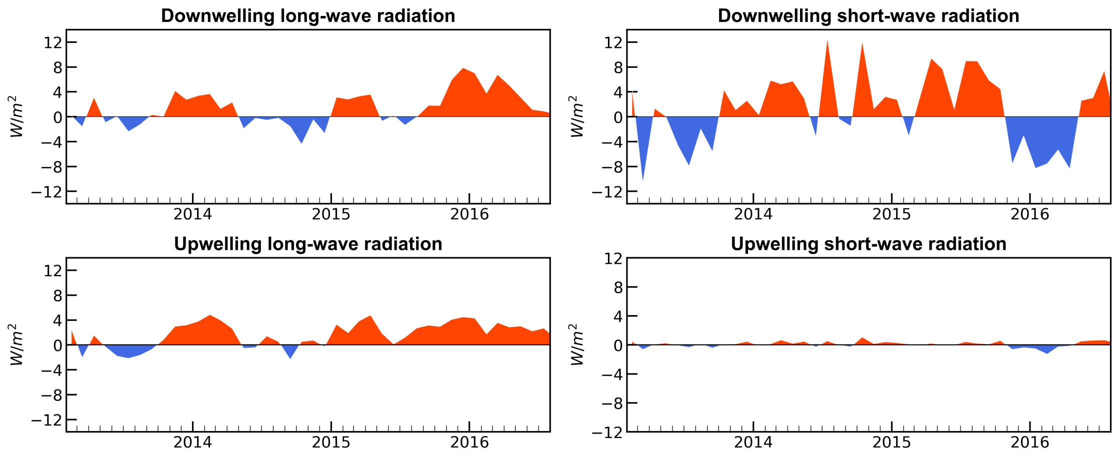

Figure S7. Radiative flux anomalies during the Pan-Caribbean drought observed from the NASA's CERES data. As expected during dry intervals, there is an increase in incoming short-wave radiation likely due to lower than normal cloud cover. However, during the recent Pan-Caribbean drought anomalously high incoming long-wave radiation was observed, which is mostly due to the rise of anthropogenic greenhouse gas concentrations, with an averaged departure of 0.8 W m^{-2} between January 2013 and December 2016 (as estimated relative to the 2001–2016 CERES climatology).

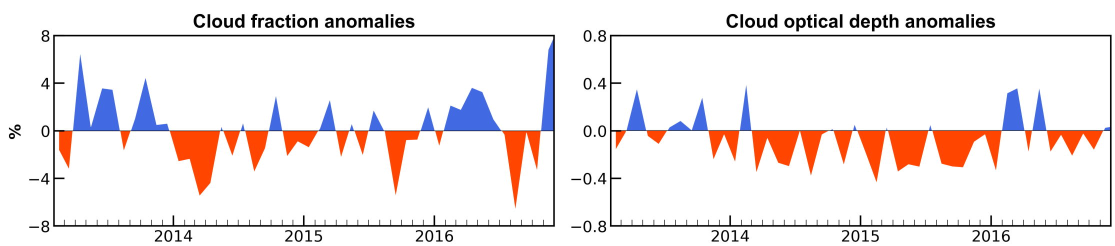

Figure S8. Cloud fraction and cloud optical depth anomalies during the Pan-Caribbean drought observed from the NASA's CERES data. During the Pan-Caribbean drought a below-normal cloud fraction is observed across the Caribbean. However, the persistent decrease in deep convection, as evaluated from below-normal cloud optical depth anomalies, is the main characteristic of the drought. As in FIG. S6 we estimated these anomalies as departures from the 2001–2016 CERES climatology.

SUPPORTING TABLES

Table S1. Observed climate datasets.

Variable	Dataset	Native resolution	Period used	Reference
Precipitation	*GPCC	1º	1949–2016	Schneider et al. (2014)
	*CHIRPS	0.05º	1981–2016	Funk et al. (2015)
	*CRU TS4.01	0.5º	1949–2016	Harris et al. (2014)
	WorldClim (Climatology)	~1 km	1950–2000	Hijmans et al. (2005)
	*CHELSA (Climatology)	~1 km	1979–2013	Karger et al. (2016)
Temperature	*BEST	1º	1949–2016	Rohde et al. (2013)
	*NCEP–NCAR Reanalysis	2.5º	1949–2016	Kalnay et al. (1996)
	*CRU TS4.01	0.5º	1949–2016	Harris et al. (2014)
	WorldClim (Climatology)	~1 km	1950–2000	Hijmans et al. (2005)
Net radiation	*JRA-55 Reanalysis	~1.25º	1958–2016	Ebita et al. (2011)
	*NCEP–NCAR Reanalysis	~1.8º	1949–2016	Kalnay et al. (1996)
	*CRU TS4.01	0.5º	(Climatology)	Harris et al. (2014)
	*CERES	1º	2001–2016	Loeb et al. (2012)
Wind speed	*NCEP–NCAR Reanalysis	2.5º	1981–2010 (Climatology)	Kalnay et al. (1996)
	*CRU TS4.01	0.5º	1949–2016	Harris et al. (2014)
Vapor pressure	Derived from *BEST	1º	1949–2016	Rohde et al. (2013)
	*CRU TS4.01	0.5º	1949–2016	Harris et al. (2014)
Elevation	WorldClim	~1 km	- -	Hijmans et al. (2005)
Available Water Holding Capacity	*IGBP–DIS	0.08º	- -	Global Soil Data Task Group (2000)
Radiative fluxes	*CERES	1º	2001–2016	Loeb et al. (2012)

***GPCC: Global Precipitation Climatology Centre Version 7.**
***CRU: Climatic Research Unit version TS4.01**
***CHIRPS: Climate Hazards Group InfraRed Precipitation with Station data.**
***CHELSA: Climatologies at High resolution for Earth's land Surface Areas.**
***BEST: Berkeley Earth Surface Temperature.**
***NCEP–NCAR: National Centers for Environmental Predictions–National Center for Atmospheric Research.**
***IGBP–DIS: International Geosphere-Biosphere Programme Data and Information Services.**
***CERES: Clouds and Earth's Radiant Energy Systems.**
***JRA-55: Japanese 55-year Reanalysis.**

Table S2. List of the CMIP5 models used in this work. From these models, we use monthly means of daily maximum and minimum temperature data at 2 m (tasmax and tasmin, respectively), radiation data (rlds, rlus, rsds, and rsus), and soil moisture data (mrso) from historical period (1949–2005), RCP8.5 (2006–2016), and pre-industrial control (1949–2016). We use one member from each model.

Model	**Resolution (lat./lon.)**	**Variables used**								
		Tasmx	**Tasmin**	**Pr**	**Rlds**	**Rlus**	**Rsds**	**Rsus**	**mrso**	**sfcWind**
BCCM-CSM1-1-M	1.1215° x 1.125°	x	x	x						
CESM1-BGC	0.9424° x 1.25°	x	x	x						
CESM1-CAM5	0.9424° x 1.25°	x	x	x						
CNRM-CM5	1.4008° x 1.4063°	x	x	x	x	x	x	x	x	x
CNRM-CM5-2	1.4008° x 1.4063°	x	x	x	x	x	x	x		x
CMCC-CESM	3.711° x 3.75°	x	x	x						
CMCC-CM	0.7484° x 0.75°	x	x	x						
CMCC-CMS	1.8652° x 1.875°	x	x	x						
GFDL-CM3	2° x 2.5°	x	x	x						
GFDL-ESM2G	2.0225° x 2.5°	x	x	x						
GFDL-ESM2M	2.0225° x 2.5°	x	x	x						
GISS-E2-H	2° x 2.5°	x	x	x						
GISS-E2-R	2° x 2.5°	x	x	x						
GISS-E2-H-CC	2° x 2.5°	x	x	x						
GISS-E2-R-CC	2° x 2.5°	x	x	x						
HADGEM2-CC	1.25° x 1.875°	x	x	x	x	x	x	x	x	x
HADGEM2-ES	1.25° x 1.875°	x	x	x	x	x	x	x		x
INMCM4	1.5° x 2°	x	x	x	x	x	x	x	x	x
IPSL-CM5A-LR	1.8947° x 3.75°	x	x	x	x	x	x	x	x	x
IPSL-CM5A-MR	1.2676° x 2.5°	x	x	x	x	x	x	x		x
IPSL-CM5B-LR	1.8947° x 3.75°	x	x	x	x	x	x	x	x	x
MIROC-ESM-CHEM	2.7905° x 2.8125°	x	x	x	x	x	x	x	x	x
MIROC-ESM	2.7905° x 2.8125°	x	x	x	x	x	x	x	x	x
MRI-CGCM3	1.1215° x 1.125°	x	x	x	x	x	x	x	x	x
MPI-ESM-LR	1.8652° x 1.875°	x	x	x	x	x	x	x	x	x
MPI-ESM-MR	1.8652° x 1.875°	x	x	x	x	x	x	x	x	x
MRI-ESM1	1.1215° x 1.125°	x	x	x	x	x	x	x		x
NORESM1-M	1.8947° x 2.5°	x	x	x						
NORESM1-ME	1.8947° x 2.5°	x	x	x						

Table S3. Relative changes in drought area over land: *"% of land affected"* refers to the percentage of land under each drought category; *"% relative contribution"* refers to the estimated relative anthropogenic contribution to the area of each drought category; while *"Total land area"* is the area of each island/region obtained or calculated from CIA (2013).

Region/Island	**Mild-drought area (scPDSI between –1.00 and –1.99)**		**Severe-drought area (scPDSI between –3.00 and –3.99)**		**Total land area (km^2)**
	Percentage of land affected	***Percentage relative contribution***	***Percentage of land affected***	***Percentage relative contribution***	
Caribbean*	67	7	28	20	239681
Cuba	59	18	22	25	109820
Hispaniola	76	6	33.5	23	76420
Jamaica	65	11	25.9	24	10831
Lesser Antilles*	39	19	37.85	13	9236
Puerto Rico	68	9	13.6	22	8870

* Not including Trinidad and Tobago and Barbados.